Modeling support of functional relationships between capillary pressure, saturation, interfacial area and common lines

Rudolf J. Held, Michael A. Celia *

Environmental Engineering and Water Resources Program, Department of Civil and Environmental Engineering, Princeton University, Princeton, NJ 08544, USA

Abstract

Computational pore-scale network models describe two-phase porous media flow systems by resolving individual interfaces at the pore scale, and tracking these interfaces through the pore network. Coupled with volume averaging techniques, these models can reproduce relationships between measured variables like capillary pressure, saturation, and relative permeability. In addition, these models allow nontraditional porous media variables to be quantified, such as interfacial areas and common line lengths. They also allow explorations of possible relationships between these variables, as well as testing of new theoretical conjectures. Herein we compute relationships between capillary pressure, saturation, interfacial areas, and common line lengths using a pore-scale network model. We then consider a conjecture that definition of an extended constitutive relationship between capillary pressure, saturation, and interfacial area eliminates hysteresis between drainage and imbibition; such hysteresis is commonly seen in the traditional relationship between capillary pressure and saturation. For the sample pore network under consideration, we find that hysteresis can essentially be eliminated using a specific choice of displacement rules; these rules are within the range of experimental observations for interface displacements and therefore are considered to be physically plausible. We find that macroscopic measures of common line lengths behave similarly to fluid–fluid interfacial areas, although the functional dependencies on capillary pressure and saturation differ to some extent. © 2001 Elsevier Science Ltd. All rights reserved.

Keywords: Network modeling; Porous media; Two-phase flow; Constitutive relationships

1. Introduction

Recent efforts to develop a comprehensive framework for multi-phase flow from first principles have included derivation of conservation equations for phases, interfaces, and common lines at the macroscale, a length scale of tens to hundreds of pore diameters [10,12,13,16,40]. Interfacial areas in multi-phase systems have been incorporated explicitly in thermodynamic theories as new independent macroscopic variables (see Refs. [9,10,12,16,34] and references cited therein). Common lines of three phases are present at the contact of three interfaces; these also enter into multi-phase flow equations, and may play a role in the movement of fluids and interfaces [9]. While these new theories indicate that interfaces and common lines should be incorporated into mathematical descriptions, the relative importance of these variables remains to be explored.

Experimental measurement techniques that are able to resolve and quantify phase interfaces in porous media systems are under development (e.g., Refs. [22,25,33,39]), but difficulties remain in the procedures and in the evaluation of indirect measurements of interfacial areas. Kim et al. [25] point out that for the partitioning traces techniques an independent validation of the interfacial area estimates is currently not available. There have been no definite studies of hysteresis cycles or scanning curves involving experimental determination of interfacial areas; recent studies report such information for a drainage sequence alone (Refs. [22,39], Montemagno, 1999, private communication). Experimental quantification of the contact lines formed at the intersection between interfacial areas and the solid has yet to be attempted. Given the difficulties associated with measurements of these variables in the laboratory or in the field, numerical simulations may play an important role in evaluating these new theories.

Numerical techniques can be employed to quantify phase interfaces (e.g., Refs. [23,31,36,37]). In this paper,

---

* Corresponding author.

we also include the quantification of common lines, starting with an idealized description of the pore microstructure in a porous medium representation. Pore-scale network models, based on capillary-dominated displacement mechanisms, provide explicit calculations of interfacial areas, as well as capillary pressures, saturations, and relative permeabilities. These models represent the pore space by geometric approximations to individual pore elements, while maintaining the highly interconnected nature and random size distributions of natural porous media. Numerical network models with various pore-space representations have been employed to investigate many phenomena related to multi-phase flow in porous media, including several recent papers investigating interfacial areas in multi-phase flow. Lowry and Miller [31], using an irregular network structure of spherical nodes and cylindrical tubes, reported relationships between fluid saturation and fluid–fluid interfacial areas. Reeves and Celia [37] developed a network model consisting of spherical pores and constricted (bi-conical) cylindrical tubes in a regular cubic network, and related interfacial areas to both capillary pressure and saturation. Fenwick and Blunt [8] investigated wedge and corner flows with an angular representation of pore throats within a network model. A similar approach was taken by Kawanishi et al. [23] with a cubic lattice arrangement of pores and tubes with triangular cross-sections to estimate interfacial areas in a three-fluid-phase system. These authors compared their network model predictions of air–water interfacial areas with the adsorption tracer estimates of effective interfacial areas obtained by Kim et al. [24]. Reported interfacial areas for initial drainage of a porous medium were consistent with the experimental results, after a normalization to allow comparison between different porous media types. Their simulation results for primary drainage were also comparable with those of Reeves and Celia [37].

Reeves and Celia [37] and Reeves [36] demonstrated that specific interfacial area, defined as the fluid–fluid interfacial area per bulk volume of the porous medium, becomes a well-behaved continuum variable at the same averaging volume as fluid saturation. The computational results of [37,36] appeared to confirm the thermodynamic hypothesis of Hassanizadeh and Gray [16] that capillary pressure, saturation, and specific interfacial area are functionally related (see also Ref. [14]). Scanning curves could be presented, which fill the space between the main (or secondary) drainage and main (or secondary) imbition curves, yielding a functional form of the constitutive relation defined by capillary pressure, p^c, wetting fluid saturation, s^w, and fluid–fluid interfacial area, a^{wn}. Simple displacement rules were used for drainage and imbition processes in [37]; these displacement rules were consecutively refined to include experimentally observed physical displacement mechanisms by Reeves [36]. Herein we extend these earlier

modeling efforts by including, for the first time, explicit calculations of common line length, l^{wns}, and exploring its relation to capillary pressure and saturation. We also explore the displacement rules used in these models by examining sensitivity of results to different choices of physically justifiable rules. And we test a conjecture associated with the theories of Hassanizadeh and Gray [18] (a review is also found in Ref. [34]) regarding hysteresis by searching for a physically justifiable set of displacement rules, for which hysteresis between drainage and imbition disappears in the relationship between p^c, s^w, and a^{wn}.

We begin this paper by restating some of the recent theoretical developments in the description of multi-phase flow in porous media, which result in inclusion of interfacial areas and common lines. Our computational pore-scale network model is then presented, including an account of the displacement rules and the computation of capillary pressure, interfacial areas, and common lines. Results are presented to demonstrate the hysteresis between capillary pressure and fluid saturation; this is followed by a computational investigation of the sensitivity of the functional relationship between capillary pressure, fluid saturation, and interfacial areas with respect to displacement rule parameters. We also report computed common line lengths, demonstrate their functional dependence on capillary pressure and saturation, and investigate sensitivity to the displacement parameters. We conclude with a discussion of these results, as well as unresolved issues in the theoretical development of the two-phase flow description, and the possibilities that pore-scale network models offer to solve some of these problems.

2. Theoretical developments and conjectures

Two-phase flow systems have historically been described using fluid pressures and volumetric saturations as primary variables. Mass balance equations for each fluid phase are augmented by constitutive relationships that relate volumetric flux of a given phase to gradients of fluid potential in that phase; the coefficient of proportionality involves the relative permeability, which is usually taken to be a nonlinear function of saturation. Similarly, the capillary pressure, defined as the difference between fluid phase pressures, is related algebraically to the saturation via another nonlinear relationship, which is usually highly hysteretic. These equations represent the state of the art in mathematical descriptions of two-phase flow in porous media.

Recently, in a series of publications, Gray and Hassanizadeh [9,11,12,16–18] have pointed out a number of inconsistencies in the standard mathematical description of multi-phase flow systems, and provided theoretical arguments that point to interfacial areas as

important primary variables in the mathematical description of two-phase flow systems. Their analysis also indicates that common lines, which form at the intersections of three phases (two fluids and one solid in the case of two-phase flow in porous media), may also be important in the flow description. While these theoretical arguments are interesting, and offer the potential for improved mathematical descriptions as well as enhanced insights into the underlying physics of the flow processes, they introduce a number of new variables, many of which are difficult if not impossible to obtain in the laboratory or in field situations.

2.1. Momentum balance

To give a sense of the kinds of equations that arise in the new theories, we present below the combined macroscale momentum equations for two-phase flow in porous media, following [9,12]:

$$
\begin{aligned}
-\epsilon^{\alpha}&(\nabla\mu^{\alpha}-\rho^{\alpha}\mathbf{g}^{\alpha})+a^{\mathrm{wn}}(\nabla\mu^{\mathrm{wn}}+\rho^{\mathrm{wn}}\mathbf{g}^{\mathrm{wn}})\\
&+a^{\alpha\mathrm{s}}(\nabla\mu^{\alpha\mathrm{s}}+\rho^{\alpha\mathrm{s}}\mathbf{g}^{\alpha\mathrm{s}})-l^{\mathrm{wns}}(\nabla\mu^{\mathrm{wns}}-\rho^{\mathrm{wns}}\mathbf{g}^{\mathrm{wns}})\\
&=\mathbf{R}^{\alpha}\cdot\mathbf{v}^{\alpha\mathrm{s}}+\mathbf{R}^{\mathrm{wn}}\cdot\mathbf{v}^{\mathrm{wn,s}}+\mathbf{R}^{\alpha\mathrm{s}}\cdot\mathbf{v}^{\alpha\mathrm{s,s}}\\
&\quad+\mathbf{R}^{\mathrm{wns}}\cdot\mathbf{v}^{\mathrm{wns,s}}\quad\alpha=w,n
\end{aligned}
\tag{1}
$$

with

$$
\nabla\mu^{\alpha}=\nabla p^{\alpha}-\frac{a^{\mathrm{wn}}}{\epsilon^{\alpha}}\nabla c_{\mathrm{wn}}^{\alpha}-\frac{a^{\alpha\mathrm{s}}}{\epsilon^{\alpha}}\nabla c_{\alpha\mathrm{s}}^{\alpha},
\tag{2}
$$

$$
\nabla\mu^{\mathrm{wn}}=\nabla\gamma^{\mathrm{wn}}-\frac{\epsilon^{\mathrm{w}}}{a^{\mathrm{wn}}}\nabla c_{\mathrm{w}}^{\mathrm{wn}}-\frac{\epsilon^{\mathrm{n}}}{a^{\mathrm{wn}}}\nabla c_{\mathrm{n}}^{\mathrm{wn}}-\frac{l^{\mathrm{wns}}}{a^{\mathrm{wn}}}\nabla c_{\mathrm{wns}}^{\mathrm{wn}},
\tag{3}
$$

$$
\nabla\mu^{\alpha\mathrm{s}}=\nabla\gamma^{\alpha\mathrm{s}}-\frac{\epsilon^{\alpha}}{a^{\alpha\mathrm{s}}}\nabla c_{\alpha}^{\alpha\mathrm{s}}-\frac{\epsilon^{\mathrm{s}}\mathbf{E}^{\mathrm{s}}}{a^{\alpha\mathrm{s}}j}:\nabla\sigma^{\alpha\mathrm{s}}-\frac{l^{\mathrm{wns}}}{a^{\alpha\mathrm{s}}}\nabla c_{\mathrm{wns}}^{\alpha\mathrm{s}},
\tag{4}
$$

$$
\nabla\mu^{\mathrm{wns}}=\nabla\gamma^{\mathrm{wns}}-\frac{a^{\mathrm{wn}}}{l^{\mathrm{wns}}}\nabla c_{\mathrm{wn}}^{\mathrm{wns}}-\frac{a^{\mathrm{ws}}}{l^{\mathrm{wns}}}\nabla c_{\mathrm{ws}}^{\mathrm{wns}}-\frac{a^{\mathrm{ns}}}{l^{\mathrm{wns}}}\nabla c_{\mathrm{ns}}^{\mathrm{wns}}.
\tag{5}
$$

In these equations, ϵ denotes the volume fraction, ρ is density, and $\mathbf{g}$ is gravity. As a convention in the employed notation, phases are referred to with indices α or β, indicating either of the phases w, n, or s; i.e., wetting, nonwetting, and solid phase, respectively. Interfaces are referred to by $\alpha\beta$ for any pair of phases wn, ws, or ns, and consistently common line properties are indexed with wns. The terms on the left-hand side of Eq. (1) now include contributions by phase interfaces $a^{\alpha\beta}$ and common lines l^{wns}, phase pressures p^{α}, surface and line tensions γ^{wn}, $\gamma^{\alpha\mathrm{s}}$, and γ^{wns}, and coefficients c stemming from postulated thermodynamic interactions; where the solid phase has a dependence on the strain tensor $\mathbf{E}^{\mathrm{s}}$ divided by the Jacobian j in a deformation term and the stress in the αs interface due to solid deformation $\sigma^{\alpha\mathrm{s}}$. The resistance coefficients $\mathbf{R}$ on the right-hand side of Eq. (1) are derived from linearizations around velocity relations $\mathbf{v}$ in the entropy inequality. The general form of Eq. (1) may be further simplified to commonly used multi-phase-flow equations by relaxed assumptions for the derived

thermodynamic relations [9]. These assumptions then become explicit, and an improved momentum balance equation, as compared to Darcy's approximation, can be developed for more general multi-phase flow conditions.

The primary variables in Eq. (1) include specific interfacial areas $a^{\alpha\beta}$, defined as interfacial area between phase α and β per unit bulk volume, and specific common line length l^{wns}, defined as common line length between all three phases (wetting, nonwetting, and solid) per unit bulk volume. Mathematically, they may be defined as (cf. [12])

$$
a^{\alpha\beta}=\frac{1}{\delta V}\int_{\delta\mathrm{S}^{\alpha\beta}}\mathrm{d}S=\frac{\delta S^{\alpha\beta}}{\delta V}
\tag{6}
$$

and

$$
l^{\mathrm{wns}}=\frac{1}{\delta V}\int_{\delta\mathrm{C}^{\mathrm{wns}}}\mathrm{d}C=\frac{\delta C^{\mathrm{wns}}}{\delta V}
\tag{7}
$$

with δV being a representative averaging volume including all phases in the system, $\delta S^{\alpha\beta}$ the two-dimensional boundary between phases α and β, and δC^{wns} the one-dimensional contact line between interfaces, within the averaging volume δV.

These variables are extremely difficult to measure experimentally. In addition, constitutive relationships between these and other variables arise, with associated parameters appearing in the relationships. Experimental studies are required to test the validity of these theoretical results and to quantify coefficients in relationships that are found to be valid. While the ideal solution is to perform careful, detailed experiments in the laboratory, our inability to measure many of the variables involved precludes this as a viable option. Therefore it is reasonable to consider numerical experiments, to the extent that they can predict some of the postulated functional dependencies and test some of the conjectures.

2.2. Constitutive relations

An implication that arises from this theory is that capillary pressure must have a functional dependence on more than just saturation. In particular, the thermodynamic analyses indicate that capillary pressure should be related to saturation, specific interfacial areas, and perhaps specific common line length in a dynamic equation that usually takes the general form of (following Ref. [9])

$$
\frac{M_{\mathrm{s}}^{\mathrm{w}}}{\epsilon}\frac{\mathrm{D}^{\mathrm{s}}s^{\mathrm{w}}}{\mathrm{D}t}=p^{\mathrm{w}}-p^{\mathrm{n}}+p^{\mathrm{c}}(s^{\mathrm{w}},a^{\mathrm{wn}},a^{\mathrm{ws}},a^{\mathrm{ns}},l^{\mathrm{wns}}),
\tag{8}
$$

where $M_{\mathrm{s}}^{\mathrm{w}}$ is a relaxation coefficient, and $\mathrm{D}^{\mathrm{s}}/\mathrm{D}t$ is a material derivative with respect to the motion of the solid phase.

A full functional relationship between capillary pressure, saturation, and fluid–fluid interfacial area has

yet to be measured experimentally, due to the difficulties associated with such measurements. However, techniques have been developed recently that should allow for such measurements to be performed (see e.g., Ref. [22,25,33,39] and references to earlier work). Until such measurement techniques are fully developed, one may use computational pore-scale models to quantify these variables and examine their functional relationships (see Refs. [23,36,37]). We follow the approach of pore-scale modeling herein to look at several specific questions, including the conjecture by Gray and Hassanizadeh related to hysteresis in postulated constitutive relations for two-phase flow systems. Hysteresis is ubiquitous in the relationship between capillary pressure and saturation, occurring for virtually all natural porous media. Gray and Hassanizadeh conjecture that hysteresis between capillary pressure and saturation is a result of the absence of specific fluid–fluid interfacial area in the functional relationship; that is, the standard relationship between capillary pressure and saturation is a projection of a three-dimensional surface relating p^c, s^w, and a^{wn} onto the two-dimensional plane with p^c and s^w as the axes. Using a computational pore-scale network model for capillary displacement in porous media, we can investigate this conjecture to determine whether or not we see a basis for rejection of the conjecture. We do this in the following sections. Furthermore, we use the computational model to examine the functional dependencies of specific common line length, in particular the relationship between l^{wns}, p^c, and s^w.

3. Numerical modeling

In multi-fluid porous media, fluid–fluid interfaces exist at the pore scale. The deformation and displacement of these interfaces allow for changes in saturation, typically in response to changes in fluid pressures. If we want to investigate the role of phase interfaces and the role of contact lines, it is logical to begin at the pore scale. For natural porous media, the geometry of the pore space is too complex to allow for a practical mathematical model, even if the geometry could be measured. Pore-scale network models attempt to capture the general features of the pore structure, while using simplified local geometries that allow for computationally tractable methods and incorporation of the relevant physics of the problem. Typically this involves a lattice representation of the pore space, with pore bodies at the vertices and pore throats acting as connections between adjacent pore bodies. Reviews of computational pore-scale network models may be found in Refs. [1,7,38]. With general averaging techniques (e.g., Ref. [15]), upscaling of displacement and flow processes to a macroscopic scale allows macro-scale flow formulations and associated constitutive relationships to be evalu-

ated. The mathematically constructed pore network acts as surrogate for an actual sample of a porous medium. On this sample, we perform experiments that mimic those that we might perform in a laboratory; however, the network model allows us to quantify variables like interfacial areas and contact line lengths, which we are unable to measure in the laboratory.

Natural porous media have inherent randomness associated with the pore structure. Randomness is assigned to the pore geometry in the model by selection of pore sizes from representative probability distributions. The pore structure of the model used herein is a regular cubic lattice of pore bodies connected by pore throats (see Refs. [36,37]). Pore bodies are spherical, while pore throats have a converging–diverging conical shape (also used in e.g., Refs. [35,41]). The radii of the pore throats are correlated in size to the adjacent pore bodies, following the procedure of Reeves [36]. Site-bond correlation leads to the overlap of the pore-body and pore-throat size distributions, and threshold pressures at comparable magnitudes for piston displacement and snap-off in imbibition processes. Such pore space correlation has been employed in pore-network models, for example, to simulate physical behavior observed in mercury porosimetry [2,6,19,30,43,46]. The wetting and nonwetting fluids are assumed to be in contact with the respective fluid reservoir at the top and bottom of the model domain. Lateral boundaries are closed to flow, as a representation of standard pressure cell experiments. Pressures at each of the fluid reservoirs can be specified in the model; changes in pressure lead to redistribution of the fluid phases via interface motions until an equilibrium distribution, i.e, a stable configuration of fluid–fluid interfaces inside the pore network, is reached. The simulated displacement mechanisms are detailed below. The fluid physical and chemical parameters correspond to an air–water system that is strongly water wet, such that contact angle hysteresis is not included. All fluids are assumed to be incompressible. Further specification of the model input parameters is provided in Table 1.

3.1. Interface displacement

The pore-scale computational model simulates quasi-static fluid displacement, such that only the end points of interface motions from one stable configuration to another are considered. Interface displacements are driven by imposed phase pressures in the fluid reservoirs; changes in the imposed pressure in one of the fluid phases will cause movement of at least some of the interfaces in the network. The mathematical rules we use for interface displacements are consistent with physical experiments in which interface motions have been studied, which are typically two-dimensional etched-glass micromodel studies [3–5,20,26–29,44,45]. Under drainage conditions, the main displacement mechanism

Table 1
Model input parameters used for all simulations

Lattice network parameters
Lattice dimensions: $40 \times 40 \times 40$
Averaging dimensions: $30 \times 30 \times 40$ (reduced by five lateral shells)
Lattice spacing (mm): 0.3
Lattice element statistics (beta distributed):

Element radii:	Mean	S.D.	Cv (–)	Min	Max
Pore bodies (mm)	0.0940	0.0141	0.1498	0.0509	0.1200
Pore throats (mm)	0.0587	0.0087	0.1481	0.0340	0.0835
Mean aspect ratio	0.162×10				

Element surfaces:	Total	
Pore bodies (mm^2)	0.4962×10^3	(6.61% of total)
Pore throats (mm^2)	0.7005×10^4	(93.38% of total)

Element volumes:	Total	
Pore bodies (mm^3)	0.8711×10^2	(28.49% of total)
Pore throats (mm^3)	0.2185×10^3	(71.50% of total)

Lattice statistics (reduced lattice):
Solid-void area (mm^2): 0.7502×10^4
Lattice volume (mm^3): 0.9720×10^3
Pore volume (mm^3): 0.3056×10^3
Porosity (%): 31.4492

Fluid parameters
Contact angle advancing (degrees): 0.0
Contact angle receding (degrees): 0.0
Contact angle equilibrium (degrees): 0.0
Surface tension (N/m): 0.0730
Wetting fluid density (kg/m^3): 0.9980×10^3
Nonwetting fluid density (kg/m^3): 0.1200×10

considered is piston displacement through pore throats. When the pressure difference between the two fluids is increased, so that the capillary pressure increases, all interfaces are interrogated to determine whether or not they will remain stable in their current positions. The test is based on local conditions at the interface, and follows the basic equation for capillary stability. For an interface that is free to move (that is, not part of a trapped fluid phase region), a pressure difference across the interface given by p^c will require an interface curvature given by γ^{wn}/R, where R is the radius of curvature of the interface. In the presence of a solid, the appropriate test for displacement involves comparison of the equilibrium radius R_{eq} with the actual radius of the pore throat, where R_{eq} is given by (e.g., Ref. [7])

$$R_{eq} = \frac{2\gamma^{wn}|\cos(\Theta + \Phi)|}{p^c} \qquad (9)$$

with Θ being the wetting fluid contact angle formed with respect to the pore wall, and Φ being the angle of the pore wall in the spatial coordinate system. When contact angle hysteresis is considered, commonly a receding contact angle during drainage, Θ_{rec}, and an advancing contact angle during imbibition, Θ_{adv}, are distinguished.

Interfaces that are unstable are tracked through the network, until a stable location (that is, a small enough

pore throat) is reached, or until they reach an open domain boundary. During this process, regions of wetting fluid that become completely surrounded by invading nonwetting fluid are identified as possibly trapped wetting fluid. While this identification is included in our algorithms, for the results presented herein, we do not include wetting-phase trapping. This is consistent with the assumption of strong wettability, i.e., wetting films and wedges provide continuity of wetting phase throughout the network. A secondary drainage mechanism is included to deal with single pore throats that contain wetting fluid, with the connecting pore bodies on either side of the throat containing nonwetting fluid. These so-called singlets of wetting fluid are allowed to drain, if the interface menisci penetrate the pore throat to such an extent that the two interfaces intersect. In this case we assume singlet rupture, and the pore throat becomes occupied with nonwetting fluid.

Imbibition is a more complex displacement process, and experimental observations have established two potentially important mechanisms besides piston displacement. These involve the process called snap-off, as well as the influence of local fluid configurations on displacement pressures for piston motion, schematically shown in Fig. 1. The reason that imbibition is more complex is due in part to the fact that the imbibition
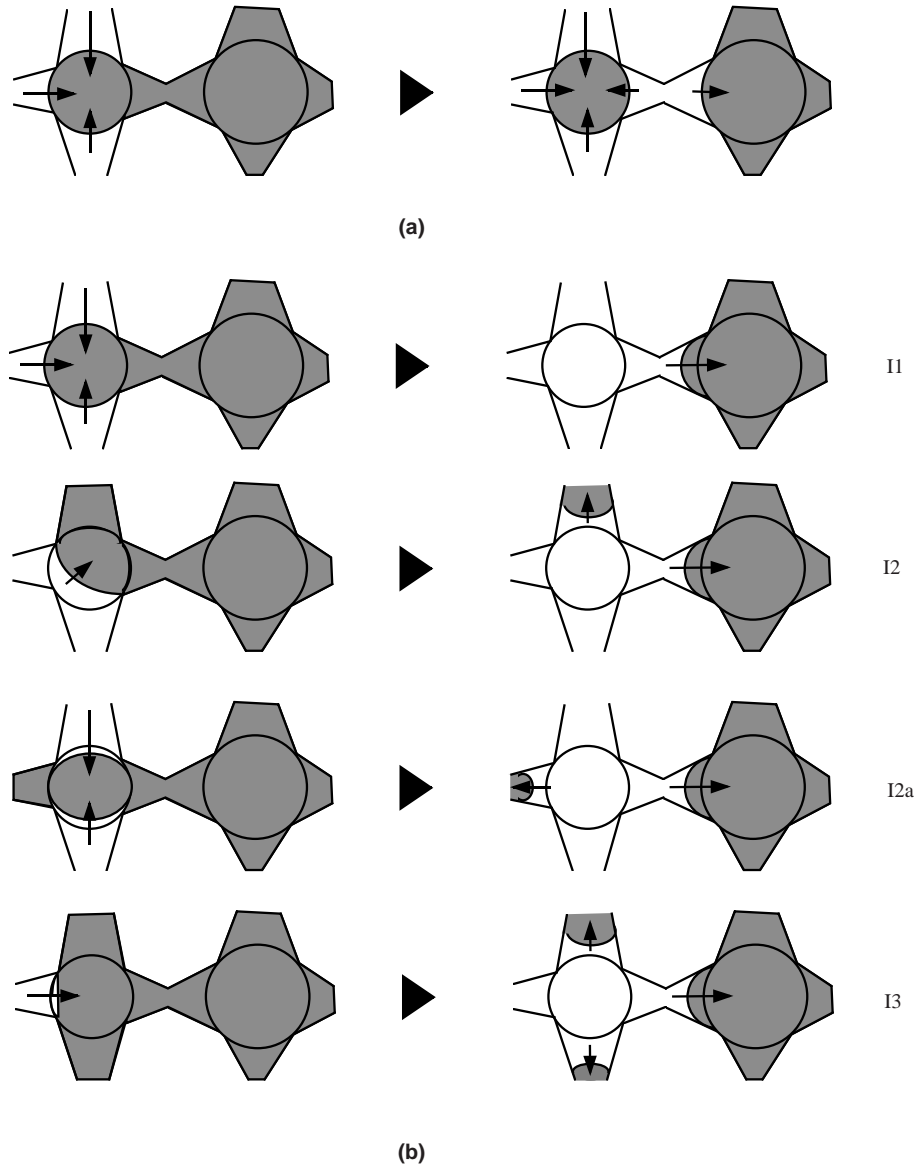
Fig. 1. Schematic of displacement rules. (a) Snap-off of nonwetting phase during imbibition. (b) Influence of local fluid configuration on cooperative pore filling during imbibition (cf. Ref. [27]). The wetting fluid in these figures is white, nonwetting fluid is shown in gray. Note that we consider local fluid configurations in three dimensions, and we do not distinguish between different configurations of the same number of connected nonwetting phase throats.

process is controlled by the pore bodies, rather than the pore throats. Pore throats have only two entrance or exit points, one on either end, whereas pore bodies have six possible entrance or exit points (in a cubic lattice). In addition, because pore throats are smaller in radius than pore bodies, and because imbibition takes place in smaller pore elements first, it is possible for wetting fluid to displace nonwetting fluid in a pore throat before it fills the intervening pore body. This latter process, referred to as snap-off or choke-off, requires wetting films and wedges to provide hydraulic connections for wetting fluid across the network. An extensive literature exists analyzing and quantifying the snap-off mechanism (see

[4,5,19,26–29,32,42,45] and references cited therein). A snap-off criterion was chosen by Reeves [36] to match the measurements of Li and Wardlaw [28], with a snap-off ratio of 1.5 for a contact angle of 0 during imbibition, and a linear parameterization for higher contact angles. The relatively general rule for snap-off in pore throats is given in Ref. [36] in terms of a snap-off parameter f_{snap}, such that the capillary pressure at which a pore throat of radius R_t will be invaded by wetting fluid is

$$p^n - p^w \leqslant \left(\frac{1}{f_{snap}} \right) \frac{2}{R_t} \gamma^{wn} \cos(\Theta_{adv}) \tag{10}$$

with Θ_{adv} denoting the advancing contact angle with respect to the solid measured through the wetting phase. In the current work, we assume $\Theta_{adv} = 0$ and allow the value for f_{snap} to vary within the range of plausible values, based on experimental evidence reported in the literature. The range of f_{snap} that corresponds to experimental observations is from 1.2 to more than 10.0 [26,27]; more characteristic for strongly wetted systems is a range found between 1.5 and 3.0 [5,28]. Li and Wardlaw [29] and Mohanty et al. [32] described a critical aspect ratio of R_b/R_t, a minimum pore-body to pore-throat size ratio, which makes snap-off possible. This criterion is related to the critical capillary pressure ratio between piston displacement and snap-off in a pore throat (see Ref. [27]), which is expressed herein with the parameter f_{snap}. For snap-off to be allowable, the stability of the resulting interface configuration is tested in our model. If the newly formed interfaces would intersect and coalesce, snap-off in that situation does not occur.

Piston-type imbibition of pore bodies involves displacement analogous to displacement for drainage in pore throats. However, the more complex geometry of the pore bodies means that factors other than the radius of the pore body may affect the imbibition process. A number of experimental studies have indicated that the capillary pressure at which imbibition occurs in a pore body is influenced by the number of pore throats connected to that pore body and that are already filled with wetting fluid (see e.g., Refs. [20,26,27,29]). Accordingly, simple piston displacement only applies to imbibition of pore bodies, where all pore throats except one are filled with wetting fluid. When more of the pore throats are filled with nonwetting fluid, then the capillary pressure condition for invasion is modified. Several models have adopted a simple correction factor for the displacement equation (e.g., Refs. [19,21,36]). Herein we follow a generalized form of the formulation by Reeves [36], for the effects of local fluid configuration, given by

$$p^n - p^w \leqslant \left(\frac{1}{f_{local}}\right) \frac{2}{R_b} \gamma^{wn} \cos(\Theta_{adv}), \tag{11}$$

where f_{local} is generalized as

$$f_{local} = wN_t + (1-w), \quad w \in [0,1]. \tag{12}$$

The parameter f_{local} depends on the number of adjacent throats filled with nonwetting fluid, N_t, weighted by a weighting factor w between 1.0 and 0.0; w corresponds to a value of 1.0 used in Ref. [21], 0.25 in Ref. [36], and 0.0 in Refs. [31,37]. Again, we chose $\Theta_{adv} = 0$ and allow different possible values of w in this study. Thus the formulation for cooperative pore filling does not take wettability into account explicitly, as we assume a strongly wetted system and a contact angle of 0 for drainage and imbibition.

For capillary displacements during imbibition, the wetting fluid sequentially invades pore throats and pore bodies with the highest capillary pressure thresholds. Piston invasion has a critical capillary pressure higher than snap-off, and thus is more probable to occur, but it requires the adjacent pore body or throat to be already filled with wetting phase [8]. The critical capillary pressure for piston-type pore filling of pore bodies is dependent on the local fluid configuration of the pore throats in strongly wetted systems. This is discussed by Lenormand and Zarcone [26]. Since pore throats are required to be narrower than the pore body to which they are connected, piston-type imbibition is always favored over snap-off in pore bodies. Thus the above displacement mechanisms are intrinsically linked to the pore structure of the model, and in turn to hysteresis in capillary displacement. Jerauld and Salter [21] determined the ratio of pore body to pore throat radii as the most important feature for observed patterns of hysteresis. The local aspect ratio in the pore structure controls imbibition capillary mechanisms that generate the fluid phase distributions.

3.2. Calculation of volumes, areas, and lines

In the overall model, phase pressures are controlled by specification of reservoir pressures. Sequential changes to the pressures produce a series of capillary pressures. For each imposed capillary pressure, interfaces are displaced within the network, employing the rules described above. Once all interfaces have reached stable locations, fluid volumes are calculated. These fluid volumes include conical sections, spheres, and spherical caps. Division of the fluid volume by the total pore volume provides a measure of fluid saturation. Note that the capillary pressure and associated saturation provide one datapoint in the traditional relationship between capillary pressure and saturation. Moreover, specific interfacial areas and specific contact line lengths are computed. Specific interfacial areas are obtained by summing all interfacial areas within the network, then dividing by the total volume of the sample. Similarly, specific common line lengths are computed by summing all of the contact lines and dividing by the total volume. Example results are shown in Fig. 2, for parameters $f_{snap} = 1.5$ (in Eq. (10)) and $w = 0.25$ (in Eq. (12)). Notice that hysteresis is present in all these relationships shown, while the overall behavior of the functional relationships is also apparent.

Specific interfacial areas have been calculated from pore-scale network models by Lowry and Miller [31], with a range of 1.4–2.0 mm²/mm³, and Reeves [36], with a range of 0.6–1.6 mm²/mm³. Kawanishi et al. [23] found the specific interfacial area for capillary menisci in a two-fluid system quantitatively similar to that of Reeves and Celia [37] at approximately 0.3 mm²/mm³
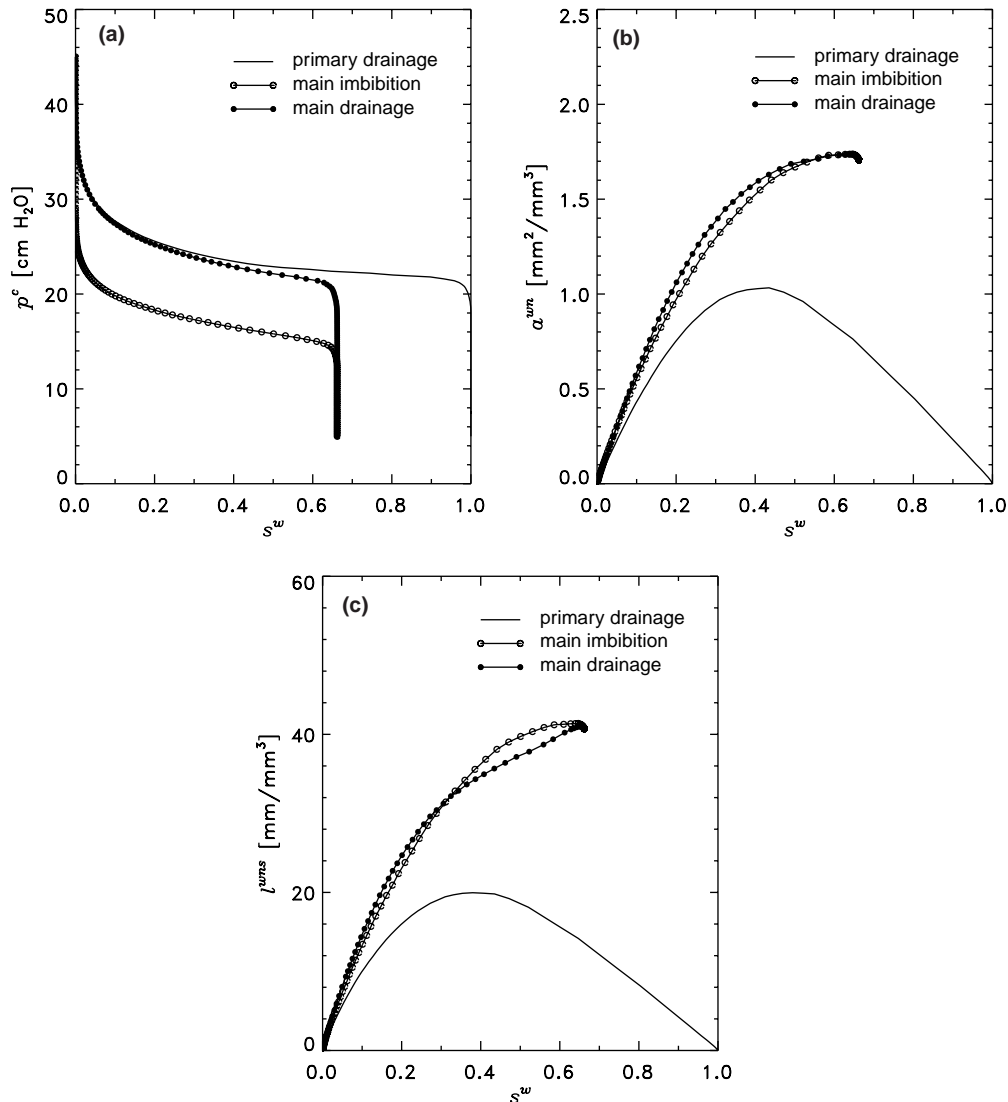
Fig. 2. Simulation of primary drainage and main hysteresis loop (snap-off parameter = 1.5, weighting in local imbibition parameter = 0.25). (a) Capillary pressure versus wetting phase saturation. (b) Specific wetting phase–nonwetting phase interfacial areas versus wetting phase saturation. (c) Specific common line length versus wetting phase saturation.

for primary drainage (after normalization with respect to the different length scales of the porous media). However, the specific interfacial area of wetting layers in their study contributed at least that much area in addition. For this investigation, we only consider interfaces between the bulk fluids, not those of wetting layers or thin films formed in corners, crevices, or pendular ring geometries.

4. Results

In this section, we present numerical results that test the conjecture that hysteresis disappears when the p^c–s^w relationship is expanded to include interfacial area between the two fluid phases. Our approach is to use the

pore-scale network model to simulate sequences of drainage and imbibition, such that complete sets of scanning curves are generated for both drainage and imbibition. We then examine the results as a function of the displacement rules used for both snap-off and the local fluid configurations. The following question is explored: Are there displacement rules that (i) are consistent with physical experiments (that is, are in the range of experimentally observed values), and (ii) produce results for which hysteresis in the p^c–s^w–a^{wn} relationship is eliminated? If not, we have a basis for rejection of the conjecture; if so, we cannot reject it. Along with interfacial areas, we will also ask the analogous question on the measure of specific contact line length.

The numerical experiments proceed as follows. Displacement of water (as the wetting phase) by air (as the

nonwetting phase), in an initially water saturated network, was simulated for a sequence of pressure steps imposed at the nonwetting phase fluid reservoir. For any combination of snap-off displacement rule factor (f_{snap}) and local imbibition rule weighting (w in f_{local}), the primary drainage sequence contained the same 150 pressure steps. These same pressure steps were also used for both the main imbibition sequence and the main drainage sequence. To fill in drainage scanning curves, the imbibition sequence was terminated prior to complete invasion and drainage was then followed to completion. Use of a sequence of termination points along the imbibition curve provides a family of drainage scanning curves that span the entire hysteresis loop. The analogous procedure was followed for imbibition scanning curves. Overall, the drainage scanning sequences contained a total of 16,106 pressure steps, and the im-

bibition scanning sequences a total of 15,960 steps. Thus every full displacement calculation amounted to simulation of 32,516 pressure steps.

4.1. Hysteresis between drainage and imbibition

Fig. 3 shows the influence of the displacement rules on the hysteresis in the p^c–s^w plane, using snap-off values of 1.0, 1.5, and 3.0. In Fig. 3(a) snap-off dominates the displacement, leading to a collapse of the main imbibition and main drainage curves on top of each other. This eliminates hysteresis between p^c and s^w, but in an unrealistic way. This result is obtained independently of the value selected for the local imbibition rule. Fig. 3(b) depicts a hysteresis loop between main imbibition and main drainage curves, which is qualitatively consistent with the observed data for porous media. This results
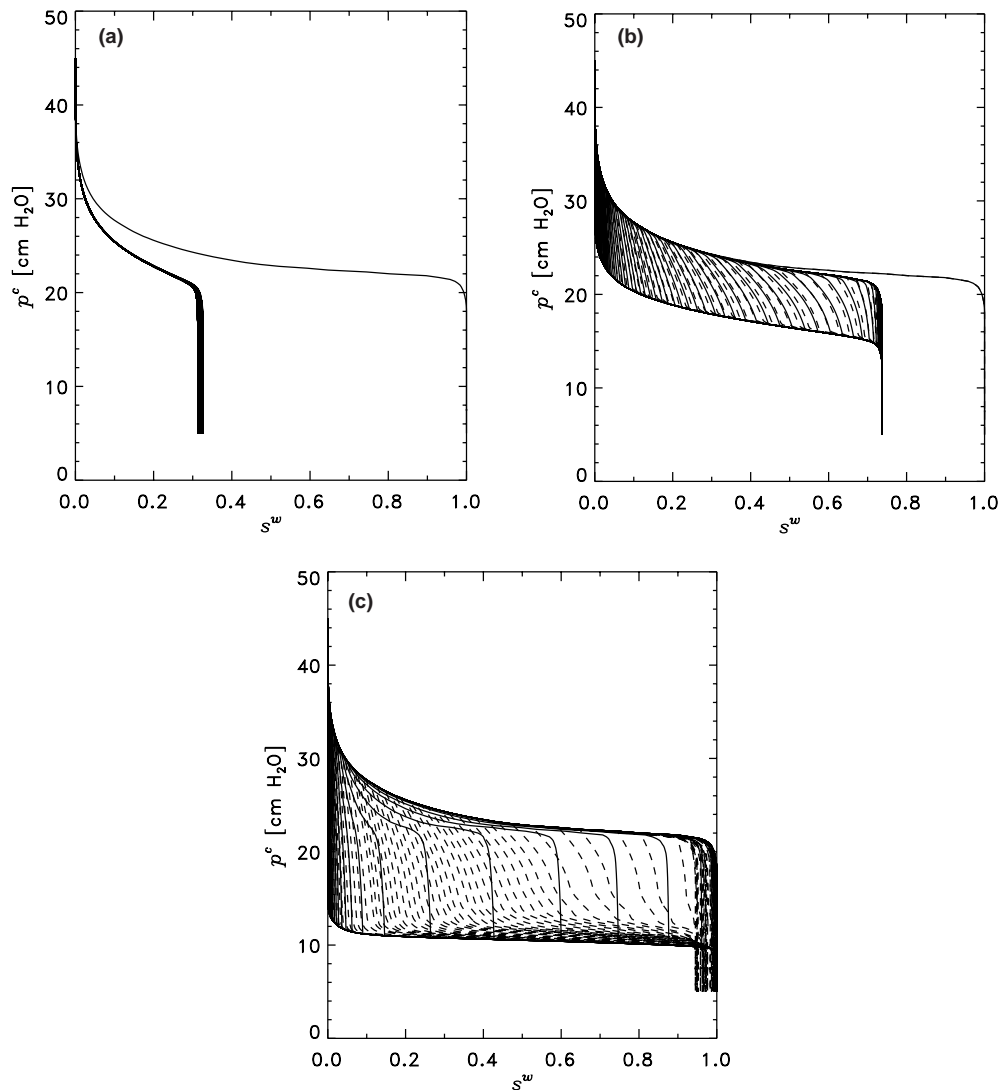

Fig. 3. Simulation of primary drainage, main hysteresis loop, and drainage and imbibition scanning curves, shown in the p^c–s^w plane. (a) Snap-off parameter = 1.0, weighting in local imbibition parameter = 0.25. (b) Snap-off parameter = 1.5, local imbibition parameter = 0.0. (c) Snap-off parameter = 3.0, local imbibition parameter = 0.25. Drainage scanning curves are given with solid lines, imbibition scanning curves with dashed lines.

from the snap-off parameter set to $f_{snap} = 1.5$, while local imbibition is weighted with $w = 0$ in this plot. The scanning sequences for drainage, i.e, starting drainage at an intermediate point on the main imbibition curve, and scanning sequences in the imbibition, i.e., starting at an intermediate point in the main drainage curve, are shown in the plot to fill the interior of the main hysteresis loop. Fig. 3(c) is an example of a high snap-off factor in combination with local imbibition weighting of 0.25. With little to no snap-off, the main hysteresis loop in the p^c–s^w plane becomes larger, producing close to no trapping of the nonwetting fluid and an unrealistically flat main imbibition curve. These illustrations of the effects of the displacement rules indicate that some of the extreme displacement parameter combinations may be ruled out as unphysical, based on unrealistic p^c–s^w curves and hysteresis behavior.

The relative importance of snap-off mechanisms to cooperative pore filling during imbibition is described using Eqs. (10) and (11) with the ratio $f_{snap}R_t : f_{local}R_b$, where the mean aspect ratio for the sample is $\langle R_b/R_t \rangle = 1.62$, given in Table 1. We examine a range of parameter values for the two imbibition mechanisms for

the fixed pore structure we have chosen. Note that the two mechanisms differ in that snap-off may occur at any pore throat in the network, whereas local fluid configurations are interrogated at the displacement front. Given the dependence of snap-off and piston displacement on the pore-size distribution, we expect to see interesting interplay of snap-off and cooperative pore filling when the f_{snap} and w parameters lead to ratios that are similar to R_b/R_t.

The full set of calculated drainage scanning cycles, along with primary and main drainage and imbibition curves, can be plotted for the relationship between p^c–s^w–a^{wn} and p^c–s^w–l^{wns}, delineating constitutive surfaces in the three-dimensional spaces (Fig. 4(a) and (b)). We provide projections of the three-parameter relationships onto the two-parameter planes in these illustrations as well. The displacement rules used in these figures correspond to a snap-off parameter of 1.5 and local imbibition weighting of 0.25 (cf. Ref. [36]), identical to the rules taken for Figs. 2 and 5 below. The drainage scanning curves for the specific interfacial area, a^{wn}_{dr} in Fig. 4(a), exhibit a pronounced curvature inside the main hysteresis loop. This convex curvature is well be-
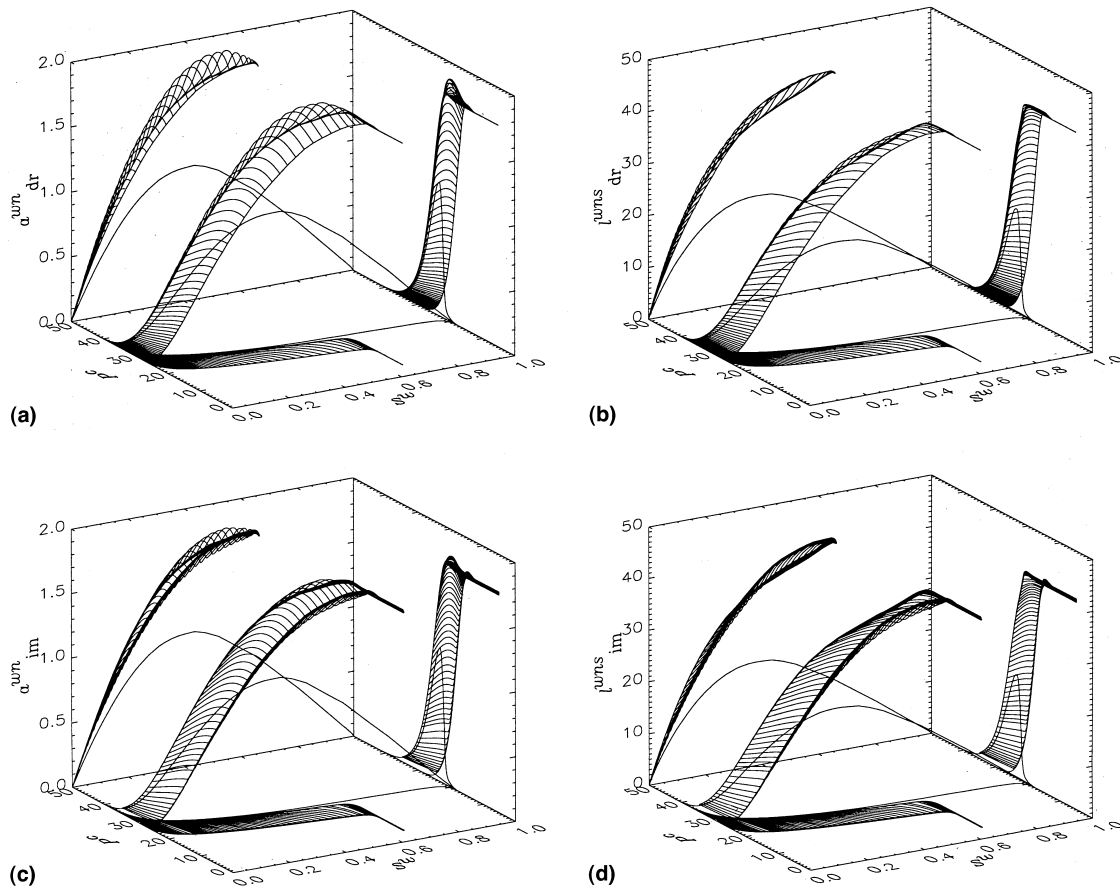

Fig. 4. Simulation of drainage and imbibition scanning curves, shown for p^c–s^w–a^{wn} and p^c–s^w–l^{wns} (see text for further explanation) (snap-off parameter = 1.5, weighting in local imbibition parameter = 0.25). (a) Drainage scanning curves for a^{wn}. (b) Drainage scanning curves for l^{wns}. (c) Imbibition scanning curves for a^{wn}. (d) Imbibition scanning curves for l^{wns}.
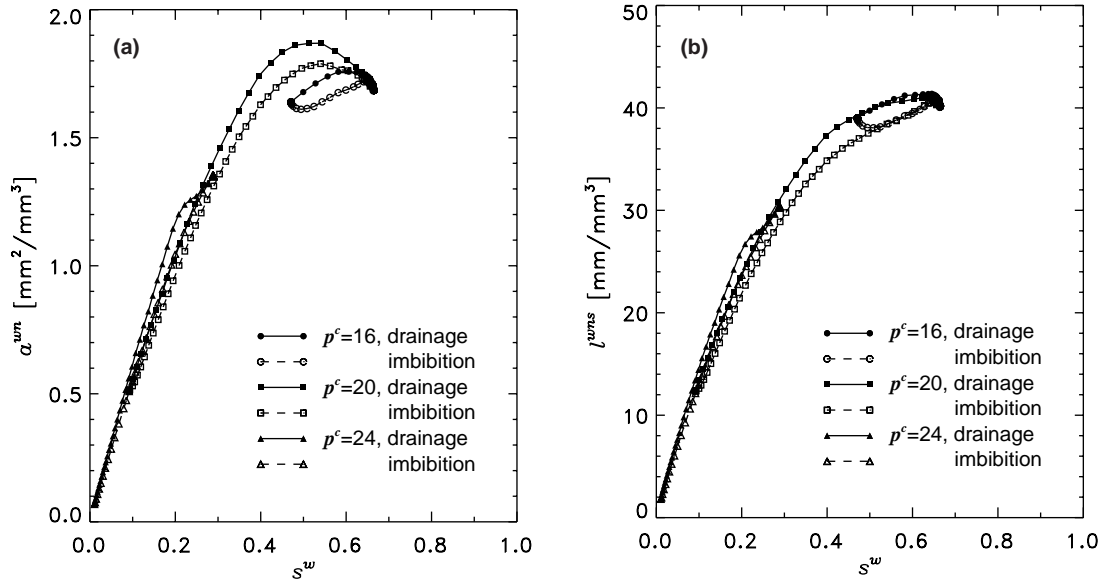
Fig. 5. Planes at constant p^c through: (a) the simulated p^c–s^w–a^{wn} and (b) p^c–s^w–l^{wns} relationships generated by drainage and imbibition scanning curves (compare to Figs. 2(a) and 4) (snap-off parameter = 1.5, weighting in local imbibition parameter = 0.25).

haved, and the curvature is highest at the high values of a_{dr}^{wn} in main drainage and main imbibition. In comparison, the drainage scanning curves for the specific common line length, l_{dr}^{wns} in Fig. 4(b), exhibit less curvature in the surface. The surfaces of the p^c–s^w–l^{wns} relationship are generally less complex, with only mild dependence of l^{wns} on p^c.

Imbibition scanning cycles for the specific interfacial area, a_{im}^{wn}, are plotted in Fig. 4(c). Primary and main drainage, as well as main imbibition curves, correspond to those in the previous figures. Projections of the scanning surface onto the two-dimensional planes are again provided for better illustration. At high interfacial area values, the imbibition scanning surface has a convex–concave curvature and a slight shift in the boundaries of the hysteresis loop between consecutive imbibition cycles. The corresponding imbibition scanning cycles for the specific common line length, l_{im}^{wns}, show the same slight shift in the boundaries of the hysteresis loop, yet a relatively flat constitutive surface (Fig. 4(d)). This is consistent with the common line drainage scanning surface, l_{dr}^{wns}, in Fig. 4(b).

When the above collection of corresponding scanning curves is cut at a fixed value of p^c, we obtain a visually easier comparison of the drainage and imbibition surfaces. Such comparison of the surfaces addresses our question of inherent hysteresis in the three-parameter representation of the constitutive relationships. Fig. 5(a) compares surface cuts for the specific interfacial area relation, and Fig. 5(b) compares surface cuts for the specific common line relation. The fixed p^c values are a sampling of the capillary pressure range inside the main hysteresis loop. The separation between drainage and imbibition displacements is less than 7% in a^{wn}, and less

than 6.5% for l^{wns}, with respect to the highest values in each plot. It is also seen in Fig. 5 that imbibition scanning sequences lie consistently below drainage scanning sequences, for this example. Furthermore, at low values of s^w, scanning sequences converge towards each other, i.e, displaying little to no hysteresis in this range in the calculated surfaces.

4.2. Parameter sensitivity

While the previous results indicated relatively mild hysteresis, it is difficult to say whether or not the differences are inherent or due to the selection of displacement rule parameters. In this section, we analyze the sensitivity of the network model results to the displacement rule combinations for snap-off and local imbibition weighting. The variability of the snap-off factor f_{snap} (Eq. (10)) is considered between a maximum of 2.5 [27,32], i.e, little to no snap-off in our simulations, and a minimum of 1.0, i.e., a forced snap-off condition. The physically plausible range, where also p^c–s^w relationships compare to experimental results, is certainly contained within these limiting values. The range for the local imbibition weighting w (in Eq. (12)) is selected from 1.0 weighting of local fluid configuration [21], to a zero weighting of local fluid configuration, i.e., no effect of the local fluid conditions on imbibition. Experimental observations under comparable conditions (phase wettabilities) [26,27,29] fall well within this range; a nonzero contact angle is further expected to diminish the influence of local fluid configurations [20,45].

For a quantitative comparison and analysis, it is desirable to quantify the complete surfaces for the scanning sequence calculations of a^{wn} and l^{wns}. A triangular

discretization with linear interpolation of the scanning sequence data was performed on the surfaces within the main hysteresis loop in the projection on the p^c–s^w plane, for drainage and imbibition separately. This information was then used to compute differences between the surfaces of drainage and imbibition (that is, to quantify hysteresis between these surfaces). Measures of the difference between the calculated surfaces are introduced with normalized moments of the residuals. The normalization is performed with respect to the area of the main hysteresis loop in the p^c–s^w plane, $\int_{s^w, p^c} \mathrm{d}s^w \, \mathrm{d}p^c$, such that

$$m_n^a = \left[\frac{\int_{s^w, p^c} \left\{ a_{dr}^{wn}(s^w, p^c) - a_{im}^{wn}(s^w, p^c) \right\}^n \mathrm{d}s^w \, \mathrm{d}p^c}{\int_{s^w, p^c} \mathrm{d}s^w \, \mathrm{d}p^c} \right]^{1/n}$$
$$n = 1, 2 \qquad (13)$$

and

$$m_n^l = \left[\frac{\int_{s^w, p^c} \left\{ l_{dr}^{wns}(s^w, p^c) - l_{im}^{wns}(s^w, p^c) \right\}^n \mathrm{d}s^w \, \mathrm{d}p^c}{\int_{s^w, p^c} \mathrm{d}s^w \, \mathrm{d}p^c} \right]^{1/n}$$
$$n = 1, 2. \qquad (14)$$

Eq. (13) corresponds to the first and second moments from the drainage and imbibition scanning sequences for specific interfacial areas, a_{dr}^{wn} and a_{im}^{wn}, and Eq. (14) applies to common line lengths, l_{dr}^{wns} and l_{im}^{wns}. The measures of m_1 and m_2 will thus indicate whether the residuals balance out overall, and whether drainage and imbibition sequences actually coincide.

In addition to these integrated measures, where many details of the specific area and common line surfaces become lumped, we present the maximum values over the drainage and imbibition scanning sequences, $a_{max}^{wn} = \mathrm{Max}[a_{dr}^{wn}, a_{im}^{wn}]$ and $l_{max}^{wns} = \mathrm{Max}[l_{dr}^{wns}, l_{im}^{wns}]$. We have also computed the areas encompassed by the main hysteresis loop in the p^c–s^w plane, i.e., the denominators in Eqs. (13) and (14), $A_{s,p} = \int_{s^w, p^c} \mathrm{d}s^w \, \mathrm{d}p^c$. All these values are obtained for a set of parameter combinations chosen from within the ranges for the snap-off and local imbibition factors (Eqs. (10)–(12)).

Fig. 6 shows the specific interfacial area maxima, a_{max}^{wn}, for the displacement simulations in the parameter space of the displacement rules. A variability of the interfacial area maxima is noted from 1.2 to 4.1 mm²/ mm³, with the highest fluid–fluid interfacial areas generated by a dominant snap-off in the displacement. In this region of dominant snap-off, the results are insensitive to the selection of the local imbibition rule. At snap-off factors of 1.5 and larger, the influence of local imbibition conditions begins to appear and extends progressively into the parameter space as the snap-off parameter increases. This insensitivity of our results at displacements dominated by snap-off, and the increase in sensitivity to local imbibition at higher values of f_{snap}, is also found in the remaining figures in this section.
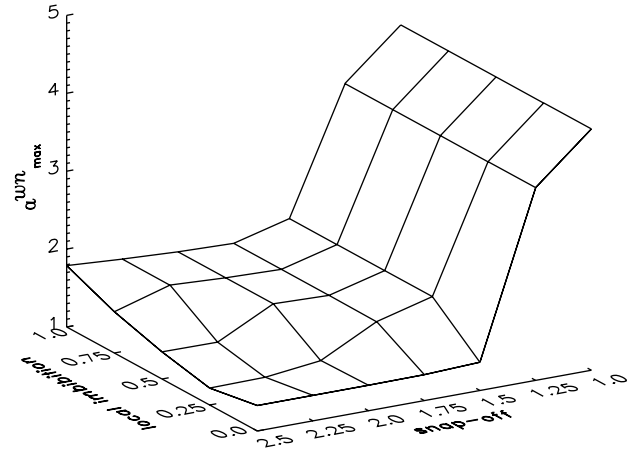

Fig. 6. Parameter space dependence of simulated displacement rules for maxima in the specific wetting phase–nonwetting phase interfacial areas, a_{max}^{wn}.

Note that, as shown in Fig. 7, $A_{s,p}$ displays an opposite trend in magnitudes to a_{max}^{wn}, with the lowest values occurring for dominant snap-off (this is consistent with the behavior described above in Fig. 3).

The first moment m_1^a for the specific interfacial areas, with units as the specific interfacial area in mm²/mm³, is given in Fig. 8(a). The positive range of m_1^a indicates drainage processes with a higher specific interfacial area than imbibition processes, and vice versa for the negative range. A projection of the contour lines is provided in the plot. The zero contour line follows the diagonal feature pointed out above, and marks the locations in the parameter space where the integrated drainage surface equals the integrated imbibition surface. It does not necessarily mark the elimination of hysteresis between the scanning curve surfaces. For example, it is observed at high snap-off values along the zero contour line that the drainage surface cuts the imbibition surface twice, at low wetting phase saturation values and high wetting
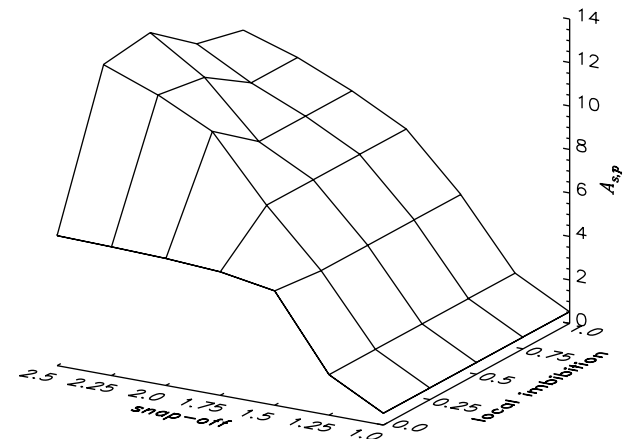

Fig. 7. Parameter space dependence of simulated displacement rules for hysteresis in the p^c–s^w projections, $A_{s,p}$.
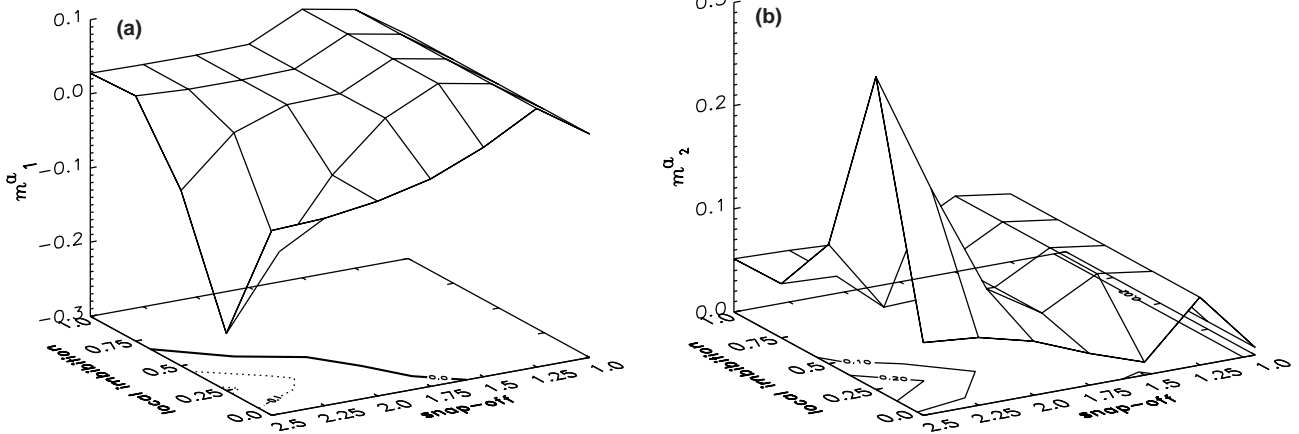
Fig. 8. Parameter space dependence of simulated displacement rules on hysteresis. (a) First moments for specific wetting phase–nonwetting phase interfacial areas. (b) Second moments for specific wetting phase–nonwetting phase interfacial areas.
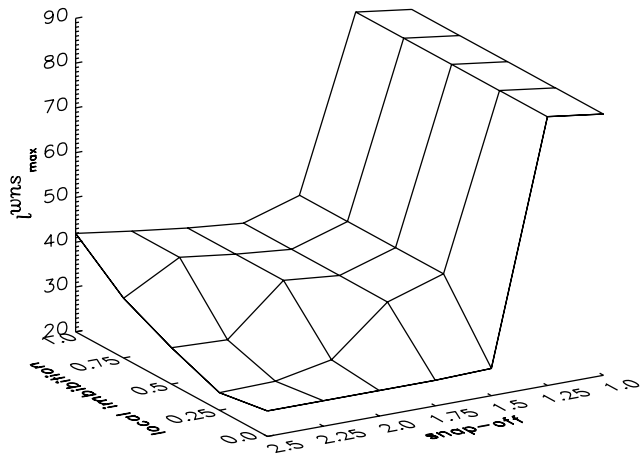

Fig. 9. Parameter space dependence of simulated displacement rules for maxima in the specific common line lengths, $l_{\max}^{wns}$.

phase saturation values. The second moment m_2^a in Fig. 8(b) reveals where the difference between the two surfaces a_{dr}^{wn} and a_{im}^{wn} is de facto minimized, as seen at the location corresponding to the end of the zero contour line, at $f_{snap} = 1.5$ and $w = 0$. The other minimum region, at a snap-off parameter of 1.0, corresponds to a lack of hysteresis in the p^c–s^w plane, and thus unphysical conditions in two-phase capillary displacement (see Fig. 3(a)).

Figs. 9 and 10 supply the analogous information of $l_{\max}^{wns}, m_1^l$, and m_2^l for the specific common line lengths ($A_{s,p}$ being identical with Fig. 7). These figures show a behavior similar to that in the corresponding figures for specific interfacial area, which is not that surprising, considering the geometric relation between common lines and interfacial area of menisci in our model. The values of $l_{\max}^{wns}, m_1^l$, and m_2^l are given in mm/mm³ and are an order of magnitude higher than for the respective specific interfacial area values. The description of the zero contour lines and minima in the first and second
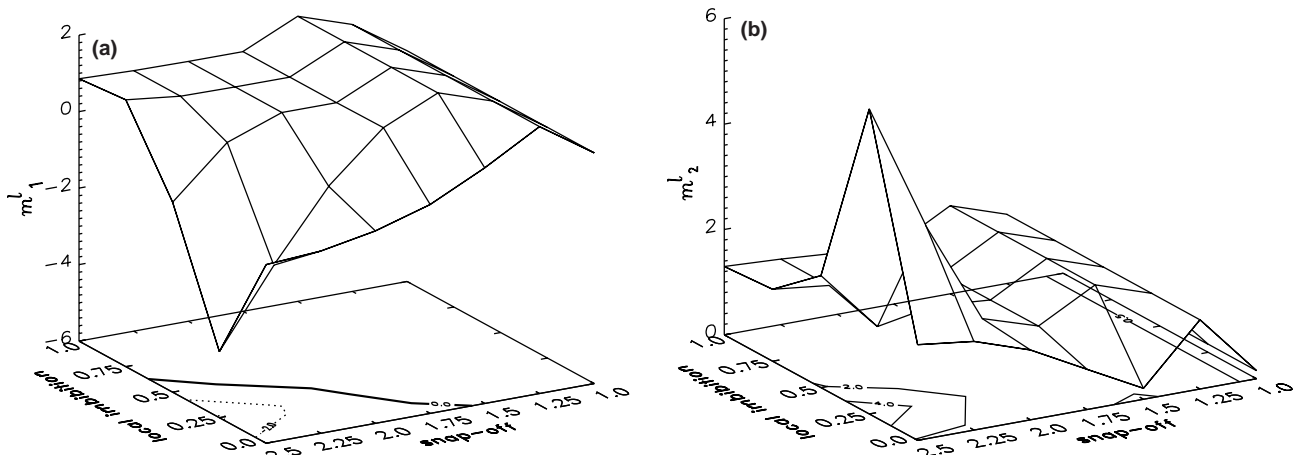

Fig. 10. Parameter space dependence of simulated displacement rules on hysteresis. (a) First moments for specific common line lengths. (b) Second moments for specific common line lengths.

moments are analogous to those for specific interfacial areas. In particular, we find one physical condition minimizing hysteresis between the common line surfaces in the neighborhood of a snap-off parameter of 1.5 and zero local imbibition weighting.

Based on these findings, we focused on the parameter space around the observed minimum of hysteresis produced by the model. We present results for specific interfacial areas only, given the similarity of results for the specific common lines. Fig. 11 displays the snap-off parameter ranging from 1.5 to 1.75, and local imbibition from 0.0 to 0.25, i.e, one grid box of the previous parameter space analysis. The wire-meshed surfaces are constructed by displacement simulations at each of the

indicated data points, as before. The first moment, shown in Fig. 11(a), offers a strikingly similar picture to Fig. 8(a), with the zero contour line cutting diagonally across the parameter domain. Fig. 11(b) also displays identical features as the plot of m_2^a in the previous parameter space (Fig. 8(b)). This indicates that the network model predictions are well behaved and allow consistent refinement in the parameter space of the displacement rules. In the final refinement of the parameter space, only the contour plots of m_1^a and m_2^a are given in Fig. 12. Parameters used as combinations of the displacement rules are labeled on the axis labels in these plots. We observe the zero contour line in Fig. 12(a) intersecting the snap-off axis close to a parameter value
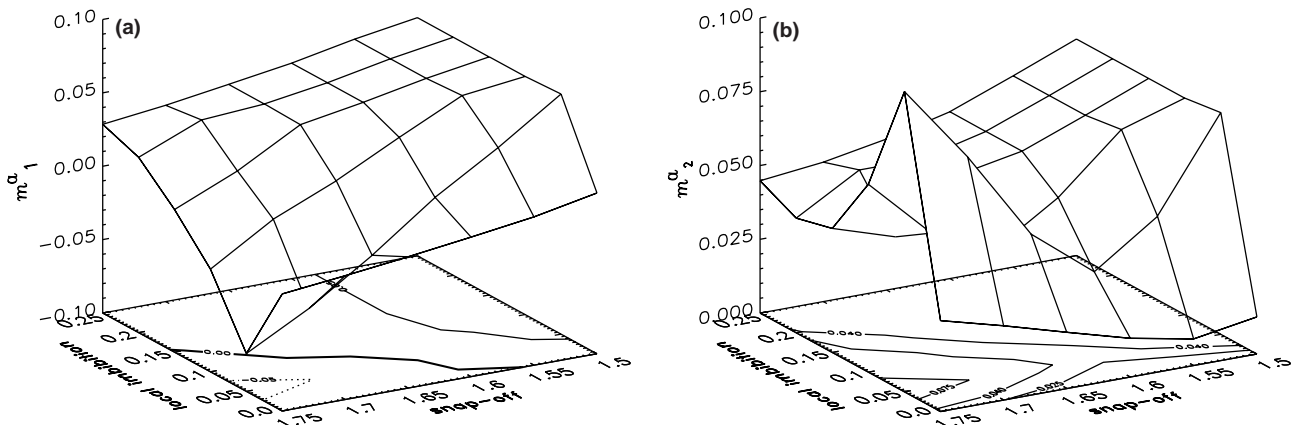

Fig. 11. Refined parameter space dependence of simulated displacement rules on hysteresis. (a) First moments for specific wetting phase–nonwetting phase interfacial areas. (b) Second moments for specific wetting phase–nonwetting phase interfacial areas.
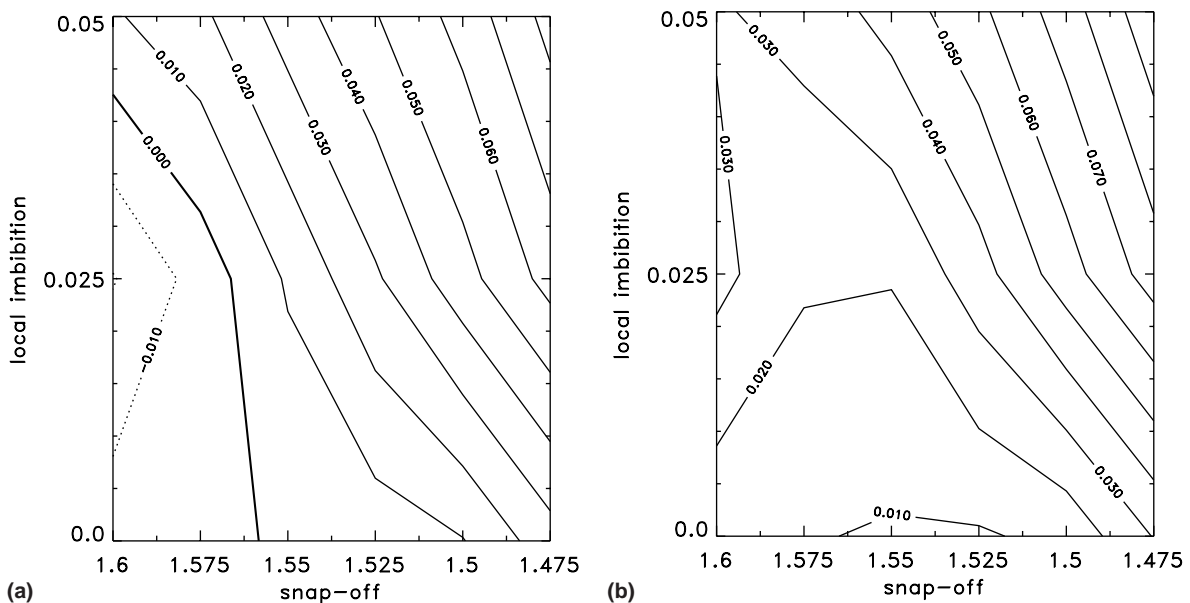

Fig. 12. Contour plots of further refined parameter space of simulated displacement rules. (a) First moments for specific wetting phase–nonwetting phase interfacial areas. (b) Second moments for specific wetting phase–nonwetting phase interfacial areas.

of 1.55. The identical location holds for the minimum in m_2^a in Fig. 12(b).

In view of the foregoing results, the hysteresis between drainage and imbibition is significantly reduced for a snap-off factor of approximately 1.55, and a local fluid configuration weighting of approximately 0. Use of these parameters produced drainage and imbibition surfaces that are very close to one another in the investigated sample, as shown in Fig. 13. For practical purposes, we may consider these results to essentially eliminate hysteresis in the p^c–s^w–a^{wn} and p^c–s^w–l^{wns} relationships.

The functional relationship of a^{wn} versus l^{wns} is depicted in Fig. 14 for both the drainage scanning curves and the imbibition scanning curves. These graphs are for the model parameters used in Fig. 13. The relationships shown in Fig. 14 are close to linear, revealing a slope of $l^{wns}/a^{wn} \sim 20$. For a single fluid–fluid meniscus, we can predict the slope of this relationship from the pore geometry, the fluid contact angle, and the equilibrium radius of the meniscus. The ratio between the interfacial area of a single fluid–fluid meniscus, A_i^{wn}, to its contact line, L_i^{wns}, is expressed by
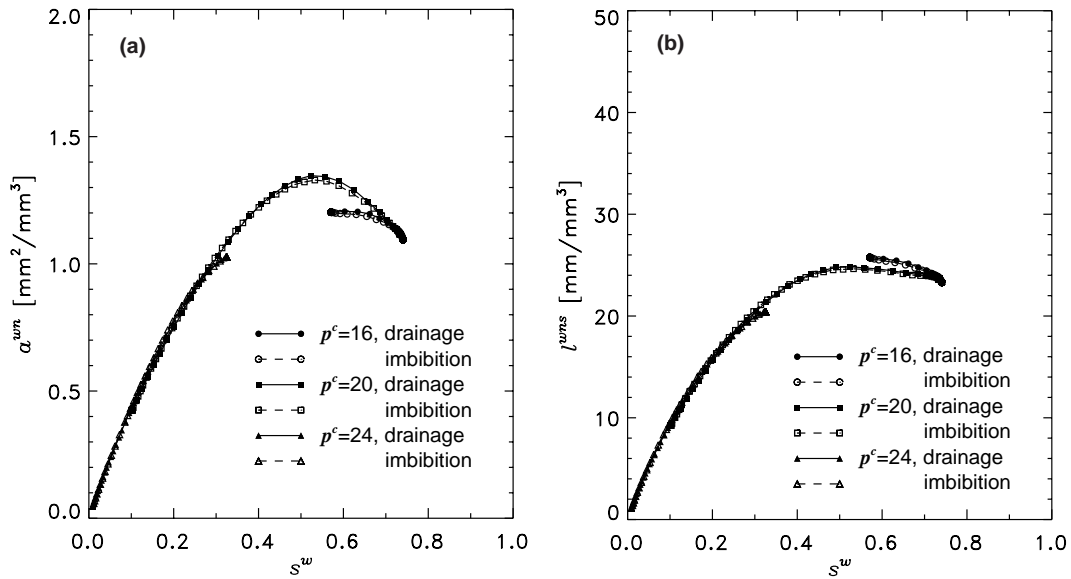

Fig. 13. Planes at constant p^c through: (a) the simulated p^c–s^w–a^{wn} and (b) p^c–s^w–l^{wns} relationships generated by drainage and imbibition scanning curves minimizing hysteresis (snap-off parameter = 1.55, weighting in local imbibition parameter = 0.0).
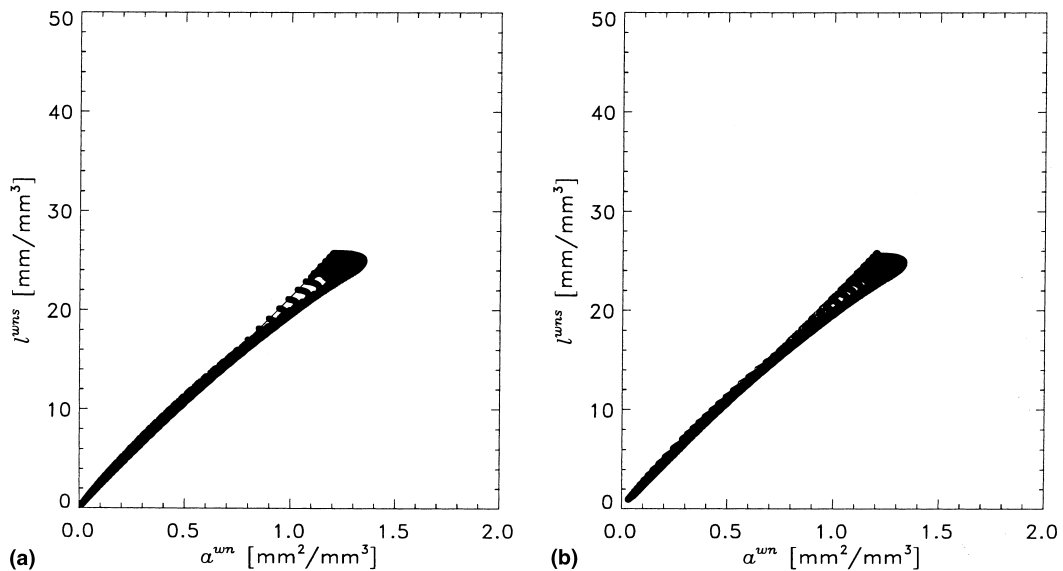

Fig. 14. Relationship of a^{wn} versus l^{wns} for the simulated scanning curves minimizing hysteresis. (a) Drainage scanning sequences. (b) Imbibition scanning sequences (snap-off parameter = 1.55, weighting in local imbibition parameter = 0.0).

$$\frac{L_{\mathrm{i}}^{\mathrm{wns}}}{A_{\mathrm{i}}^{\mathrm{wn}}} = \frac{|\cos(\Theta + \Phi_{\mathrm{i}})|}{h_{\mathrm{i}}} = \frac{\cos^2(\Theta + \Phi_{\mathrm{i}})}{R_{\mathrm{eq},i}(1 - |\sin(\Theta + \Phi_{\mathrm{i}})|)}. \quad (15)$$

For $\Theta = 0$ and average quantities for Φ and R_{eq} from the sample statistics given in Table 1, i.e, $\langle \Phi \rangle$ and $\langle R_{\mathrm{eq}} \rangle$, we obtain an estimated $l^{\mathrm{wns}}/a^{\mathrm{wn}}$ of 16–19 mm/mm^2 for the single averaging volume. The variability in the estimated slopes stems from the variation of possible menisci locations in the bi-conical pore throats. The relative simplicity of estimating this functional relationship, although it is only crudely approximated above, holds further promise. These plots suggest a clear functional relationship between model calculated a^{wn} and l^{wns}, and hints that l^{wns} may not be an important independent variable.

5. Discussion and conclusions

New theories of multi-phase flow in porous media indicate that measures of interfacial areas, and perhaps common lines, must play a role in the mathematical description of the system. However, these theoretical results cannot characterize the relative importance of these new system variables. For this, experiments are needed that can quantify the interfacial areas and common line lengths, and investigate how these variables are related to other system variables such as capillary pressure and saturation. Because the ability to measure interfacial areas and common line lengths in physical experiments remains to be developed, we have herein used numerical models to investigate the general behavior of interfacial areas and common lines. In particular, we have examined the relationship between common line length, capillary pressure, and saturation; we have examined the relationship between fluid–fluid interfacial area, capillary pressure, and saturation; we have examined the sensitivity of the results to specific choices made in the definition of pore-scale displacement rules associated with snap-off and local fluid configuration during imbibition; and we have examined the hysteresis between drainage and imbibition in the expanded functional dependencies involving interfacial areas and common line lengths. We find that hysteresis can essentially be eliminated, in the example system under consideration, with an appropriate choice of physically plausible displacement rules. This holds for both fluid–fluid interfacial areas and common line lengths. Our results imply that hysteresis in the standard relationship between capillary pressure and saturation may be due to an incomplete functional dependence, when only capillary pressure and saturation are considered. Inclusion of interfacial area, as the new theories indicate, may lead to vast reductions or even elimination of hysteresis. Below we give a discussion of some details

of our results, and indicate issues that remain to be addressed.

5.1. Functional relationships

A first observation is that with the best estimate of the displacement rule parameters from our findings, hysteresis is nearly eliminated between the drainage and imbibition surfaces for a^{wn}. The separation between these surfaces is less than 1.5% in Fig. 13(a). The functional form of the constitutive relationship between $p^{\mathrm{c}}, s^{\mathrm{w}}$, and a^{wn} appears to be well behaved, and has a relatively simple geometric shape when hysteretic effects are at a minimum. Notice that the p^{c}–s^{w}–a^{wn} surfaces enclosed by the main hysteresis loop exhibit a pronounced concave curvature in the surface for drainage and imbibition displacement processes. Hence, the relationship of p^{c} as a function of s^{w} and a^{wn} is not single-valued, and as such a theory that implies dependence of p^{c} on s^{w} and a^{wn} could be questioned. Our results indicate that the relationship of a^{wn} as a function of s^{w} and p^{c} is single-valued, so that this functional form might be the preferable choice. However, theoretical investigations remain to be performed to see if such a functional dependence is feasible.

With the best estimate of the displacement rule parameters, we found even less hysteresis in specific common line lengths, less than 1.0% (Fig. 13(b)), than we found for the specific interfacial areas. The surfaces spanned by common line lengths exhibit less curvature, especially along the p^{c} axis. The almost flat surface in the direction of p^{c} suggests that l^{wns} may not be a function of p^{c}, but only of s^{w}. Comparison of Fig. 5 with Fig. 13 also indicates that the predicted magnitudes for a^{wn} and l^{wns} from numerical modeling depend strongly on the selection of displacement parameters.

5.2. Displacement rules and hysteresis

The results presented for a specific pore-space sample may be understood in a general context. Observed hysteresis is interpreted as being caused by pore structure effects, irreversible displacement processes (Haines-jumps), and wettability effects (hysteresis of the fluid–solid contact angle) [7]. These effects have been extensively researched. The impact and interplay of the different pore-level events, determined by the pore structure, and the displacement history govern the fluid distributions (see e.g., Ref. [21]). Our results indicate that the relative influence of snap-off and piston-type retractions during imbibition contributes significantly to hysteresis in the expanded three-parameter relationships. With the displacement parameters set to physically reasonable values (based on experimental observations), the hysteresis between the drainage and imbibition surfaces is only a small percentage of the

absolute magnitude of specific interfacial areas or specific common line lengths (cf. axes in Figs. 8 and 10). The inclusion of a third variable in the constitutive relationship of p^c–s^w, i.e., the specific interfacial area between the bulk fluid phases, may be interpreted in a two-phase flow system as largely capturing the effects of irreversible processes leading to the fluid distributions.

The computational results suggest minimization of hysteresis when the snap-off parameter is in the proximity of the mean aspect ratio of the pore-network structure, and when the local fluid configuration rule is given very little weight. We can examine these results from two points of view. The first involves questioning the result regarding the local fluid configuration, whether or not this particular result is physically plausible. Hysteresis might be expected to be lowest when there is little or no effect from local fluid configurations during imbibition, since piston-type advance through pore bodies then becomes similar to a reversed drainage process. An additional remark in this regard involves the observation that when differences between advancing and receding contact angles are present, experimental observations indicate that the influence of local fluid configurations is greatly reduced [20,29]. While we did not include contact angle hysteresis in our model simulations, simply to avoid confounding any such hysteresis effects that appear in the model results, incorporation of contact angle hysteresis in the displacement rules can eliminate effects of local fluid configuration. This elimination can be seen in the work of, e.g., Reeves [36] in modeling an air–water system, where for advancing contact angles greater than 20 the effect of cooperative pore filling becomes negligible. Thus elimination of local fluid configurations in the imbibition rule may be justified, although contact angle hysteresis may need to be considered.

The second point of view that we would like to consider is whether or not the computational exercise presented herein can provide guidance in the choice of parameters for displacement rules in pore-scale network models, given that experimental results provide plausible ranges for these parameters, but do not provide unique values. These parameters are measured or calculated for specific pore geometries and phase properties, both idealized for the multi-phase systems that are typically modeled. Confronted with some arbitrariness in the selection of displacement rules, there is no a priori reason for making one choice of displacement parameters instead of another. Under these conditions, we might choose as a selection criterion the minimization of hysteresis between drainage and imbibition surfaces in the p^c–s^w–a^{wn} space. That is, a possible criterion for the selection of displacement parameters is to accept the theoretical conjecture regarding elimination of hysteresis in the expanded functional dependencies, and to impose this as a criterion for parameter identification. We rec-

ognize that this chain of arguments is based on a conjecture that has yet to be proven, but we propose this criterion as an interesting possibility which, in the absence of any other criteria, could provide solutions that are internally consistent and that respect the new theoretical formulations identifying fluid–fluid interfacial area as an important system variable.

5.3. Model extensions

The network model used in this investigation has several obvious shortcomings. First, the geometry to represent pore elements provides no means for explicit development and tracking of wedges or corners of wetting fluid. Angular cross-sections, such as triangles or rectangles, provide such geometric corners and allow for wedges of wetting fluid to be present everywhere in the network. While we used an implicit assumption of wetting-phase connectivity throughout the network, these angular geometries afford the possibility to track the influence of films or wedges more directly. Such explicit wedges may add significant fluid–fluid interfacial areas, areas which behave quite differently than the capillary interfaces between the bulk fluids whose stability dictates the fluid displacement. Whether or not these two different kinds of interfaces need to be quantified separately and treated separately in the theory, remains a question to be resolved (see also Ref. [14]). The significance of this additional area remains to be investigated.

The network model is also limited by the assumption of quasi-static displacements. No temporal evolutions are included in the model; interfaces that are unstable are simply moved to the next stable location in a series of quasi-static displacements. While this is consistent with the standard formulation of capillary pressure as an algebraic function of saturation, it is not necessarily consistent with the new theories, which indicate that capillary pressure is a thermodynamic quantity that evolves dynamically and is only equal to the difference in phase pressures when system equilibrium is reached. Therefore, if we wish to test the new theories further, dynamic displacement models will be necessary. These can be developed as an extension of our current models, with or without the modified angular geometries. The combination of explicit wedges of wetting fluid and dynamic displacement algorithms also allows for possible inclusion of slow drainage through wedges and the associated time scales for displacement of apparently trapped wetting fluid. These and a host of other kinds of calculations can provide insight into problems that remain partly or wholly unresolved.

Overall, we believe that computational network models provide an important tool to study multi-phase flow and transport in porous media. They are particularly complementary to new theoretical developments

that have evolved during the past decade and which show conclusively that nontraditional variables like specific interfacial areas need to be included in our mathematical descriptions of multi-phase systems. Until experimental methods are developed to measure these nontraditional variables, computational pore-scale network models offer the only viable tool to investigate and evaluate these new theories. Investigation of hysteresis in the extended functional space involving capillary pressure, saturation, and interfacial area is one such example of this kind of assessment.

References

[1] Celia MA, Reeves PC, Ferrand LA. Recent advances in pore-scale models for multiphase flow in porous media. U.S. Nat Rep Int Union Geophys 1991–1994. Rev Geophys 1995;33:1049–57.

[2] Chatzis I, Dullien FAL. The modeling of mercury porosimetry and the relative permeability of mercury in sandstones using percolation theory. Int Chem Eng 1985;25(1):47–66.

[3] Chatzis I, Morrow NR, Lim HT. Magnitude and detailed structure of residual oil saturation. Soc Petrol Eng J 1983;23:311–26.

[4] Chen J-D. Some mechanisms of immiscible fluid displacement in small networks. J Colloid Interface Sci 1986;110(2):488–503.

[5] Chen J-D, Koplik J. Immiscible fluid displacement in small networks. J Colloid Interface Sci 1985;108(2):304–30.

[6] Diaz CE, Chatzis I, Dullien FAL. Simulation of capillary-pressure curves using bond correlated site percolation on a simple cubic network. Transport Porous Med 1987;2(3):215–40.

[7] Dullien FAL. Porous media: fluid transport and pore structure, second ed. New York: Academic Press; 1992.

[8] Fenwick DH, Blunt MJ. Three-dimensional modeling of three phase imbibition and drainage. Adv Water Resour 1998;21(2):121–43.

[9] Gray WG. Thermodynamics and constitutive theory for multiphase porous-media flow considering internal geometric constraints. Adv Water Resour 1999;22(5):521–47.

[10] Gray WG, Hassanizadeh SM. Averaging theorems and averaged equations for transport of interface properties in multiphase systems. Int J Multiphase Flow 1989;15(1):81–95.

[11] Gray WG, Hassanizadeh SM. Unsaturated flow theory including interfacial phenomena. Water Resour Res 1991;27(8):1855–63.

[12] Gray WG, Hassanizadeh SM. Macroscale continuum mechanics for multiphase porous-media flow including phases, interfaces, common lines and common points. Adv Water Resour 1998;21(4):261–81.

[13] Gray WG, Leijnse A, Kolar RL, Blain CA. Mathematical tools for changing spatial scales in the analysis of physical systems. Boca Raton, FL: CRC Press; 1993.

[14] Gray WG, Celia MA, Reeves PC. Incorporation of interfacial areas in models of two-phase flow. In: Parlange MB, Hopmanns JW, editors. Vadose zone hydrology: cutting across disciplines. New York: Oxford University Press; 1999. p. 58–85.

[15] Hassanizadeh SM, Gray WG. General conservation equations for multi-phase systems. 1. Averaging procedure. Adv Water Resour 1979;2(3):131–44.

[16] Hassanizadeh SM, Gray WG. Mechanics and thermodynamics of multiphase flow in porous media including interface boundaries. Adv Water Resour 1990;13(4):169–86.

[17] Hassanizadeh SM, Gray WG. Toward an improved description of the physics of 2-phase flow. Adv Water Resour 1993;16(1):53–67.

[18] Hassanizadeh SM, Gray WG. Thermodynamic basis of capillary pressure in porous media. Water Resour Res 1993;29(10):3389–405.

[19] Ioannidis MA, Chatzis I. A mixed-percolation model of capillary hysteresis and entrapment in mercury porosimetry. J Colloid Interface Sci 1993;161(2):278–91.

[20] Ioannidis MA, Chatzis I, Payatakes AC. A mercury porosimeter for investigating capillary phenomena and microdisplacement mechanisms in capillary networks. J Colloid Interface Sci 1991;143(1):22–36.

[21] Jerauld GR, Salter S. The effect of pore-structure on hysteresis in relative permeability and capillary pressure. Transport Porous Med 1990;5:103–51.

[22] Karkare MV, Ford T. Determination of the air–water interfacial area in wet "unsaturated" porous media. Langmuir 1996;12(8):2041–4.

[23] Kawanishi T, Hayashi Y, Robert PV, Blunt MJ. Fluid–fluid interfacial area during two and three phase fluid displacement in porous media: a network model study. In: Proceedings of the Groundwater Quality: Remediation and Protection. Tübingen, FRG: IAHS 1998;250:89–96.

[24] Kim H, Rao PSC, Annable MD. Determination of effective air–water interfacial area in partially saturated porous media using surfactant adsorption. Water Resour Res 1997;33(12):2705–11.

[25] Kim H, Rao PSC, Annable MD. Consistency of the interfacial tracer technique: experimental evaluation. J Contam Hydrol 1999;40:79–94.

[26] Lenormand R, Zarcone C. Role of roughness and edges during imbibition in square capillaries, SPE paper 13264. In: Proceedings of the 59th Annual Technical Conference and Exhibition, Soc Petr Eng, Houston, TX, 1984.

[27] Lenormand R, Zarcone C, Sarr A. Mechanisms of the displacement of one fluid by another in a network of capillary ducts. J Fluid Mech 1983;135:337–53.

[28] Li Y, Wardlaw NC. The influence of wettability and critical pore-throat size ratio on snap-off. J Colloid Interface Sci 1986;109(2):461–72.

[29] Li Y, Wardlaw NC. Mechanisms of nonwetting phase trapping during imbibition at slow rates. J Colloid Interface Sci 1986;109(2):473–86.

[30] Li Y, Laidlaw WG, Wardlaw NC. Sensitivity of drainage and imbibition to pore structures as revealed by computer-simulation of displacement processes. Adv Colloid Interface Sci 1986;26(1):1–68.

[31] Lowry MI, Miller CT. Pore-scale modeling of nonwetting-phase residual in porous media. Water Resour Res 1995;31(3):455–73.

[32] Mohanty KK, Davis HT, Scriven LE. Physics of oil entrapment in water-wet rocks. SPE Reservoir Eng 1987;2(1):113–27.

[33] Montemagno CD, Gray WG. Photoliminescent volumetric imaging: a technique for the exploration of multiphase flow and transport in porous-media. Geophys Res Lett 1995;22(4):425–8.

[34] Muccino JD, Gray WG, Ferrand LA. Toward an improved understanding of multiphase flow in porous media. Rev Geophys 1998;36(3):401–22.

[35] Nowicki SC, Davis HT, Scriven LE. Microscopic determination of transport parameters in drying porous media. Drying Technol 1992;10(4):925–46.

[36] Reeves PC. The development of pore-scale network models for the simulation of capillary pressure–saturation–interfacial area–relative permeability relationships in multi-fluid porous media. Ph.D. Thesis, Princeton University, 1997.

[37] Reeves PC, Celia MA. A functional relationship between capillary pressure, saturation and interfacial area as revealed by a pore-scale model. Water Resour Res 1996;32(8):2345–58.

[38] Sahimi M. Flow phenomena in rocks: from continuum models to fractals, percolation, cellular automata, and simulated annealing. Rev Mod Phys 1993;65(4):1393–535.

[39] Saripalli KP, Kim H, Rao PSC, Annable MD. Measurement of specific fluid–fluid interfacial areas of immiscible fluids in porous media. Environ Sci Technol 1997;31(3):932–6.

[40] Svendsen B, Hutter K. On the thermodynamics of a mixture of isotropic materials with constraints. Int J Eng Sci 1995;33(14):2021–54.

[41] Toledo PG, Scriven LE, Davis HT. Equilibrium and stability of static interfaces in biconical pore segments. SPE Formation Eval 1994;9(1):61–5.

[42] Tsakiroglou CD, Payatakes AC. A new simulator for mercury porosimetry for the characterization of porous materials. J Colloid Interface Sci 1990;137(2):315–39.

[43] Tsakiroglou CD, Payatakes AC. Effects of pore-size correlations on mercury porosimetry curves. J Colloid Interface Sci 1991;146(2):479–94.

[44] Vizika O, Payatakes AC. Parametric experimental study of forced imbibition in porous media. Physicochem. Hydrodyn. 1989;11(2):187–204.

[45] Wardlaw NC, Li Y. Fluid topology, pore-size and aspect ratio during imbibition. Transport Porous Med 1988;3(1):17–34.

[46] Wardlaw NC, Li Y, Forbes D. Pore-throat size correlation from capillary-pressure curves. Transport Porous Med 1987;2(6):597–614.